



Stain-free mapping of polymer-blend morphologies via application of high-voltage STEM-EELS hyperspectral imaging to low-loss spectra

Hiroki Umemoto^{1,2} · Shigeo Arai³ · Hirohide Otobe¹ · Shunsuke Muto^{2,3}

Received: 13 January 2023 / Revised: 12 March 2023 / Accepted: 30 March 2023 / Published online: 17 May 2023
© The Author(s) 2023. This article is published with open access

Abstract

Polymer blends composed of multiple types of polymers are used for various industrial applications; therefore, their morphologies must be understood to predict and improve their physical properties. Herein, we propose a spectral imaging method based on scanning transmission electron microscopy (STEM) and electron energy-loss spectroscopy to map polymer morphologies with nanometric resolution as an alternative to the conventional electron staining technique. In particular, the low-loss spectra of the 5–30 eV energy-loss region were measured to minimize electron irradiation damage rather than the core-loss spectra, such as carbon K-shell absorption spectra, which require significantly longer recording times. Medium-voltage (200 kV) and high-voltage (1000 kV) STEM was used at various temperatures to compare the degrees of electron-beam damage resulting from various electron energies and sample temperatures. A multivariate curve resolution technique was used to isolate the constituent spectra and visualize their distributions by distinguishing the characteristic peaks derived from various chemical species. High-voltage STEM was more useful than medium-voltage STEM for analyzing thicker samples while suppressing ionization damage.

Introduction

Polymers are used in various fields and applications owing to their light weights and the range of characteristics imparted by polymers with various chemical and mechanical properties, which depend on the chemical constituents of the monomer units. Some fields and applications require properties that cannot be achieved with the use of a single

polymer. In such cases, ‘polymer blends’, which are obtained by mixing polymers or copolymerizing monomers with different properties, are used [1]. The physical properties of polymer blends are significantly affected by the combination of the blended polymers and their underlying morphologies, that is, how the constituent polymers are intermixed microscopically [2]. Morphology-control techniques and their evaluation are important for research and development of polymer blends.

Transmission electron microscopy (TEM) has been widely applied to evaluate the morphologies of polymer blends at the nanometer scale, and several sample preparation and imaging techniques have been developed to enable better visualization of the polymer blend substructure, which otherwise exhibit low contrast between the various species. Electron staining with strong oxidizing agents such as OsO₄ or RuO₄, in which the heavy metal reacts with certain functional groups or crystal structures in the constituent polymers, is commonly used to analyze differences between the components, particularly in selectively revealing C = C bonds, benzene rings, or amorphous parts of the crystalline polymers [3, 4]. However, this method is not applicable to all types of polymer blends; for example, in some cases, no effective electron-staining agent

These authors contributed equally: Hiroki Umemoto, Shunsuke Muto

Supplementary information The online version contains supplementary material available at <https://doi.org/10.1038/s41428-023-00786-5>.

✉ Hiroki Umemoto
umemoto.hc@om.asahi-kasei.co.jp

- ¹ Platform Laboratory for Science and Technology, Asahi-kasei Corporation, Fujii, Shizuoka 416-8501, Japan
- ² Graduate School of Engineering, Nagoya University, Chikusa-ku, Nagoya, Aichi 464-8603, Japan
- ³ Advanced Measurement Technology Center, Institute of Materials and Systems for Sustainability, Nagoya University, Chikusa-ku, Nagoya, Aichi 464-8603, Japan

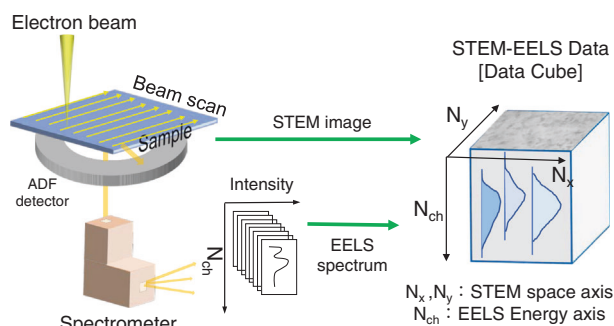


Fig. 1 Conceptual diagram of STEM-EELS-HSIA

is available, or the staining process results in very low contrast. The combination of differential phase contrast (DPC) [5] or high-angle annular dark field (HAADF) methods with scanning TEM (STEM) [6] has been proposed recently; however, these methods cannot identify the polymer species and result in degradation or interfacial reaction phases due to alloying in complex systems.

The combination of STEM and electron energy-loss spectroscopy (EELS) may resolve these issues because EELS can be used for elemental analysis and also for analyses of the chemical-bonding states in samples of interest. This technique may enable separate visualization of the spatial distributions of the underlying components in polymer blends with nanometric resolution via the collection of an EELS set as a function of the position in the sample scanned using an electron nanoprobe [7]. This method is called spectral imaging (SI), and the concept is shown in Fig. 1.

The carbon K-shell absorption spectra (C K-edge) of polymeric materials exhibit a variety of characteristic features due to the σ^* and π^* peaks, depending on the nature of the C-C bonds [8, 9], and they are very useful for distinguishing between polymer species. Isolation of the spectral features for multiple polymer components in a blend may enable effective morphological visualization [10, 11]. However, most polymers are highly susceptible to irradiation damage, which is caused by the high-energy/high-density electron illumination of S/TEM, which results in instant loss of the C K-edge features or sample perforation during measurements [12]. Therefore, the electron dose used in the measurement must be minimized to avoid sample degradation while maintaining a reasonable signal-to-noise ratio (SNR) in the spectra.

Electron-irradiation effects include knock-on damage, ionization (radiolysis), and thermal damage. Knock-on damage results from direct collisions between the incident electrons and the ion cores of the target material, which are governed by the energy/momentum conservation laws of the classical mechanics framework [13]. The energy/momentum transferred is larger for higher electron energies; however, the knock-on cross-section is smaller for higher

accelerating voltages. In contrast, ionization effects are more significant for lower accelerating voltages. Thermal damage may be caused by the thermal diffusion of atoms displaced either via knock-on or ionization and may be suppressed more effectively at lower temperatures.

We attempted to investigate the applicability of the proposed methodology, spectral changes owing to the electron irradiation, the damage suppression enabled by cooling, and differences in the damage modes for various acceleration voltages during the STEM operation. We also assessed the practicability of used high-voltage STEM for thicker polymer samples, which has never been examined.

Mapping various polymer species based on their spectral features is complex because only a few databases are available that associate peak positions to the natures of C-C bonds for a number of polymers, such as that described in [14]. In addition, only a limited number of databases have been published on the electron-irradiation damage caused by various electron doses, the accelerating voltage of the TEM used, and the sample temperatures for a wide range of polymers. A multivariate curve resolution (MCR) technique was used to analyze such SI datasets, which isolated the spectral components involved therein without a priori known reference spectra and simultaneously visualized the projected spatial distribution of each component [15]. This type of image analysis is called ‘hyperspectral image analysis (HSIA)’.

Here, we propose a stain-free method, STEM-EELS-HSIA, using low-loss (energy losses of 5–30 eV) spectra to evaluate the morphologies and local chemical states of polymer blends while minimizing electron-induced degradation. The low-loss spectra of polymers exhibit small but characteristic features as counterparts to those appearing in the C K-edge spectra [16], as well as plasmon energy shifts, which are another useful measure of material density. The low-loss spectral intensity is higher than the C K-edge spectral intensity by two or three orders of magnitude, thereby enabling a corresponding reduction in the electron dose and significantly shorter recording times.

Experimental procedure

Preparation of synthetic rubber-based polymer blends

The sample used in this study was a polymer blend containing low-density polyethylene (LDPE), thermoplastic polyurethane (TPU), and a modified hydrogenated styrene-ethylene-butylene-styrene block copolymer (SEBS). Figure 2 shows the molecular structures of the components.

LDPE (Suntec M2115) was obtained from Asahi Kasei Corporation (Tokyo, Japan), and TPU (Elastollan ET-685)

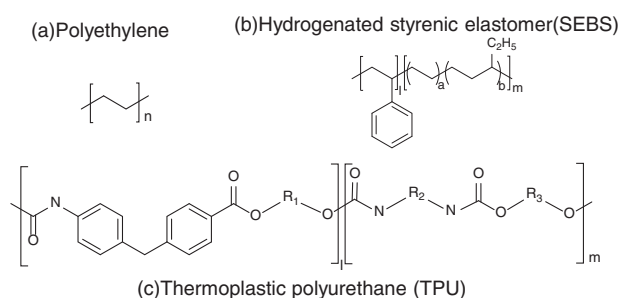


Fig. 2 Molecular structures of the components in the polymer blend sample under investigation

was procured from BASF Japan, Ltd. SEBS was synthesized according to paragraphs 149–54 of Japanese Patent No. JP2018-193431 [17]. LDPE, TPU, and SEBS were mixed at a weight ratio of 22.5:67.5:10.0 and melt-kneaded in a twin-screw extruder (TEX30, Japan Steel Works, Ltd.) at a cylinder temperature of 200 °C, screw speed of 253 rpm, and discharge rate of 5 kg/h. Then, roll forming and hydraulic press forming (200 °C, 100 kg/cm²) were used to obtain a 2 mm-thick molded sheet.

In this study, LDPE was used to reduce the weight and cost. While LDPE and TPU are incompatible (immiscible), a fine dispersion of each component at the nanometric scale is generally effective for ensuring the mechanical strength of the blend. Given its partial miscibility with both components, SEBS served as a compatibilizing agent for the LDPE and TPU.

Preparation of samples for STEM-EELS-HSIA measurements

Ultrathin sections of the polymer blend were prepared via the cryomicrotomy method using a Leica UC6 ultramicrotome and FC6 cryo-unit. The cooling temperature was set to –120 °C. Standard sections measuring 100 nm in thickness, approximately 400 μm on the long side and 150 μm on the short side, were prepared. These sections were loaded onto a Cu grid mesh without a support film for measurement. Another set of ultrathin sections was stained with Ru for TEM measurements. Ru staining was performed by placing the mesh loaded with ultrathin sections and RuO₄ crystals in the same sealed container for 4 min.

TEM and STEM-EELS-HSIA measurements

The Ru-stained sample was analyzed with an HT7700 TEM (Hitachi, acceleration voltage: 120 kV). For the STEM-EELS-HSIA measurements, two scanning transmission electron microscopes with different accelerating voltages (i.e., 200 and 1000 kV) were used: a Reaction Science high-voltage transmission electron microscope JEM-1000 K RS (JEOL, acceleration voltage of 1000 kV), which was

equipped with an energy filter (GIF Quantum equivalent), and a JEM-2100 STEM (JEOL, acceleration voltage of 200 kV), which was equipped with an EELS detector (Gatan Enfina 1000). Table 1 shows details of the STEM-EELS measurement conditions. STEM-EELS-HSIA was performed at approximately 100 K with a liquid nitrogen-cooled holder to investigate the effect of temperature on damage suppression. The incident electron-beam current was reduced, partly to improve the energy resolution (the full width at half maximum (FWHM) of the zero-loss peak (ZLP) is ~1 eV or less at 200 kV and ~1.5 eV for 1000 kV) and partly to minimize the radiation damage. The former was necessary for detecting small characteristic peaks, and the latter contributed to shortening the EELS recording time per step and, accordingly, the total data acquisition time. The spectral recording time (exposure time) per pixel was set to maximize the ZLP intensity within the detector saturation limit and the SNR for the MCR analysis; moreover, the CCD vertical binnings were set to 130 and 100 for the GIF and Enfina-1000 spectrometers, respectively, to minimize the data-transfer time of the CCD. Vertical binning deteriorates the detector dynamic range; however, the shorter total measurement time had a higher priority. Notably, the current density per pixel corresponded to a few tens of thousands of Coulombs per square meter per second, which may have significantly damaged the polymers during scanning at an accelerating voltage of 200 kV at room temperature (RT), as monitored by the π - π^* transition peak for the energy loss at approximately 5 eV [18].

The degree of thermal damage after STEM-EELS-HSIA acquisition is easily recognized in the ADF-STEM images because the scanned area appears darker than the surrounding area owing to electron irradiation-induced sample evaporation (see Fig. S1 in the Supplementary Information). As shown in Fig. S1 in the Supplementary Information, the sample measured at RT and 200 kV was significantly damaged, as expected given the electron dose per pixel. This measurement condition (200 kV/RT) was hence avoided thereafter. However, thermal damage marks do not always indicate significant thermal damage *during* the measurements because the beam scan in SI mode operates such that the probe first moves to a specified position, after which the EELS is recorded for a specific time. The electron probe remains at the same position until data transfer is complete and moves to the next position according to the specified scan step width. Thus, thermal damage occurs mainly while the probe waits after recording the spectrum because the data acquisition time per step was nearly 1 s, which was significantly longer than the spectral recording time (1 or 5 ms). Furthermore, the subpixel-scan option was selected in the present SI, so the electron probe did not remain at a point in each scan step square but scanned within the 4 × 4 subdivided areas. Therefore, the scan step

Table 1 Details of the measurement conditions

Item	Measurement conditions	
	[1]	[2]
Instrument	JEM-1000K RS (JEOL)	JEM2100 STEM (JEOL)
Accelerating voltage (kV)	1000	200
EEL spectrometer	GIF Quantum (Gatan)	Enfina 1000 (Gatan)
Probe size (nmϕ)	2	2
Exposure time (s/step)	0.005 (5/16 ms/subpixel)	0.001 (1 ms/subpixel)
Scanning step width (nm/step)	10	10
Energy dispersion (eV/ch)	0.1	0.1
Current density (pA/nm²)	10	100
CCD vertical binning	130	100
Measurement temperature	RT & 100 K	RT & 100 K

width must be sufficiently larger than the probe size to prevent the overlap of neighboring illuminated areas and suppress beam damage while accounting for beam spread in the sample. In the present study, the scan step was at least five times larger than the probe size.

Analysis of the STEM–EELS–HSIA data

Three methods were used to visualize the spatial distributions of the constituent polymers with the experimental STEM–EELS–HSIA dataset: energy filtering by selecting the spectral feature (peak) characteristic of each polymer [19], multilinear least-squares (MLLS) fitting using the standard (reference) spectra of the components [20], and MCR to isolate the underlying spectral components without a priori knowledge [21]. In the present study, MCR was first applied to the raw SI dataset, after which MLLS fitting was conducted with the unfolded spectra (endmembers) to ensure that trace components or systematic residue remains were not missed during MCR.

A STEM–EELS–HSIA dataset has a three-dimensional structure consisting of the two-dimensional spatial coordinates xy \times the spectral energy axis (Fig. 1). Among the various MCR algorithms [21], MCR via log-likelihood maximization (MCR–LLM), as proposed by Braidly et al., was recently shown to deliver statistically excellent performance [22, 23]; a brief explanation of this algorithm is given in Supplementary Information S2. We adopted this method by importing the original Python code to Gatan Microscopy Suite® (GMS) version 3.4x or higher, a commercial TEM/spectroscopy-related analysis platform, with the I/O part modified to be compatible with GMS to enable efficient and unified spectral analyses of subsequent MLLS and other fits.

Because MCR spectral decomposition requires specifying the number of components (spectra), we set this number to three, which was identical to the number of blended components. Nonlinear least-squares (NLLS) fitting was also applied

to the isolated spectra, and Gaussian functions were used to classify the peak characteristics of various chemical species.

Low-loss spectra were used to estimate the sample thickness with the Lambert–Beer law, which is expressed as follows:

$$\frac{t}{\lambda} = \ln \left[\frac{\int I(E) dE}{\int I_0(E) dE} \right],$$

where t represents the sample thickness, λ represents the electron mean free path (MFP) for plasmon loss, and $\int I(E) dE$ and $\int I_0(E) dE$ represent the total inelastically scattered and ZLP peak intensities, respectively [7]. Because λ depends on the mean atomic number and density of each constituent phase in a sample, a t/λ map can be used as a measure of the phase (polymer species) distribution, which may be used to validate the MCR results.

Results and discussion

TEM measurements with the Ru-stained sample

We first examined the morphologies of the synthetic rubber polymer blend via conventional Ru-stained TEM at RT to obtain the reference data (ground truth reference) necessary to compare them with the morphologies provided by the STEM–EELS–HSIA data.

SEBS was expected to exhibit the highest Ru-electron-staining efficiency, which would be manifested as a dark contrast in a bright-field (BF) TEM image. Among the three components, TPU showed the lowest Ru-electron-staining efficiency and the brightest contrast in the BF-TEM image. LDPE formed a mixture of amorphous and lamellar crystals at the nanometric scale [24], and the amorphous part was stained more effectively by Ru than the lamellar part. Therefore, LDPE was expected to exhibit a contrast intermediate between those of SEBS and TPU.

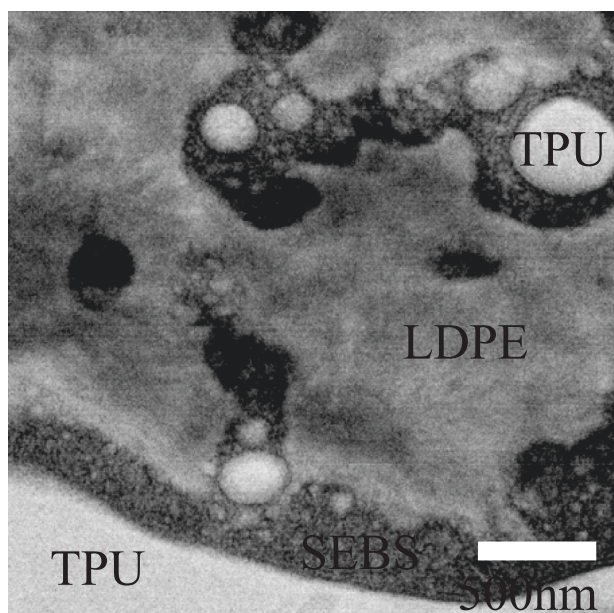


Fig. 3 TEM image of the polymer blend sample under investigation after Ru staining

Figure 3 shows a BF-TEM image of the Ru-stained polymer blend, and the components were identified based on the aforementioned principles. The sample contained circular domains, with diameters of several micrometers, dispersed in the matrix. The matrix exhibited the brightest TEM contrast, whereas the domains were classified into three contrast levels: the brightest, comparable with that of the matrix, the darkest, and an intermediate level. The areas showing these contrasts were assigned to the three blended polymers by considering the projected area ratio in the TEM image, the mixing proportion of each component during sample preparation, and the Ru-staining properties of each component. As indicated in Fig. 3, (i) the matrix and the circular domains showing the brightest contrasts corresponded to TPU, (ii) the areas showing intermediate contrast corresponded to LDPE, and (iii) the areas showing the darkest contrast corresponded to SEBS, which were mainly distributed at the boundaries between the matrix and the domains and contained smaller TPU domains with diameters of approximately 50 nm.

STEM-EELS-HSIA data for MCR-LLM analyses

Figure 4 shows the spectral components and their corresponding endmembers (spatial distributions), which were isolated with the STEM-EELS-HSIA datasets obtained under various measurement conditions with MCR-LLM, and the number of components was set at three. The result from the 200 kV/RT condition indicated significant thermal damage associated with electron irradiation (a change in the sample shape in the irradiated area, as shown in Fig. S1 in the Supplementary Information), which was excluded from

Fig. 4. The original MCR-LLM unfolding results are shown in Fig. S2 in Supplementary Information S2.

Figure 4a Summary of the MCR-LLM analysis results for the STEM-EELS-HSIA data collected under various observation conditions (1st row), ADF-STEM images (2nd row), and spatial distribution maps of the three resolved components as RGB composite images (blue: TPU; red: LDPE; green: SEBS; 3rd row). (b) Spectral endmembers corresponding to the score images in (a).

Because the same area of a sample cannot be scanned under different conditions, a direct comparison was made to determine the optimal scanning conditions. However, under all three measurement conditions, the morphologies of the polymer blends exhibited matrix-domain structures, wherein circular domains with diameters of a few micrometers were dispersed in the matrix. Based on the interpretation of the previously described Ru-stained TEM images and a comparison with the components isolated with the STEM-EELS-SI data, components 1–3, as shown in Fig. 4a, were identified as TPU, LDPE, and SEBS, respectively. All of the components exhibited similar characteristics, wherein a fine mixture of SEBS, TPU, and LDPE was distributed over the domain structure and SEBS was concentrated near the interfacial region adjacent to the matrix. The spectrum of the LDPE component exhibited the fewest $\pi-\pi^*$ transition peaks among those of the three components, which was consistent with the fact that it comprised only single bonds, unlike the other polymer species, which contained benzene ring(s) in their monomer units.

To validate the MCR results, we performed MLLS fitting of the original STEM-EELS-HSIA data cubes by using the three MCR-resolved endmembers as the basis vectors because the component spectra (endmembers) unfolded by MCR-LLM may be considered ‘calculated basis vectors (spectra)’; constraints such as nonnegativity and a fixed number of components were imposed based on the assumption that the experimental data can be expressed with a linear combination of the specified number of basis spectra (components). All of the data cubes, except those for the data collected at 200 kV/RT, wherein the sample exhibited significant thermal damage, exhibited reduced chi-squared (χ^2/σ^2 ; χ^2 : square sum of residual values, σ^2 : variance of statistical noise) values on the order of unity, as shown in Fig. S3 in the Supplementary Information. This finding validated the three-component MCR results. In addition, the nearly featureless residual images were within the accuracy of the present noise level in the residual chi-squared maps in Fig. S3 in the Supplementary Information, and this strongly indicated that no interfacial reactions (solution formation or phase separation) occurred at the interphase boundaries in the polymer blend to form residual structures. This indicated that TPU, LDPE, and SEBS, which are generally immiscible, were mixed on a

Fig. 4 a Summary of the MCR–LLM results for the STEM–EELS–HSIA data collected under various observation conditions (1st row), ADF–STEM images (2nd row), and spatial distribution maps of three resolved components as RGB composite images (blue: TPU; red: LDPE; green: SEBS; 3rd row). **b** Spectral endmembers corresponding to the score images in (a). The volume-plasmon and theoretical π – π^* transition peak positions assigned to C=C bonds are indicated

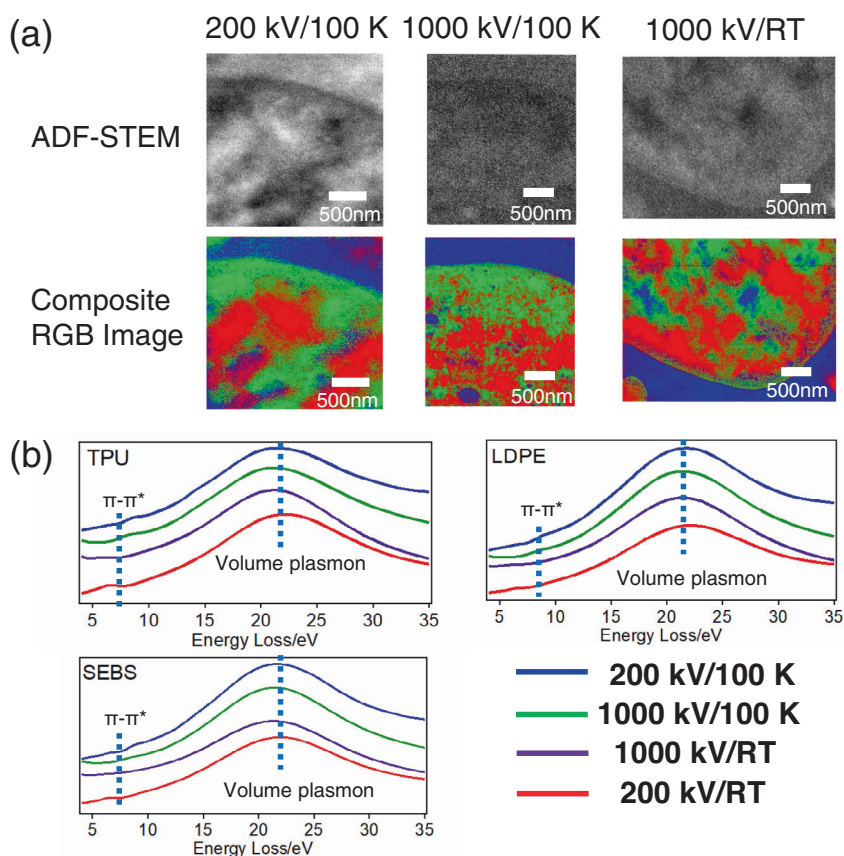
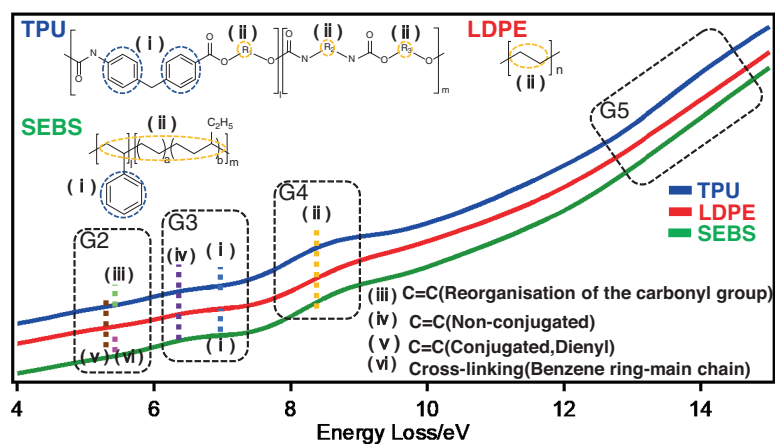


Fig. 5 Assignments of the spectral features observed at 200 kV/100 K to the specific electron transitions associated with local chemical species based on previous reports for TPU, LDPE, and SEBS



nanometric scale (semisoluble state) near the interface, owing to the ‘compatibilizing effect’ of SEBS. This was observed regardless of the temperature and accelerating voltage employed. The ADF/BF–STEM images obtained from the same areas did not present such unambiguous details, owing to their poor contrast, which proved that our methodology effectively evaluated the morphologies of the polymer blends without electron staining.

An examination of the isolated peaks shown in Fig. 4b indicated that the peak positions of the volume plasmon (~22 eV) and small characteristic peaks (5–10 eV) depended

on the electron energy and sample temperature. This finding suggested that irradiation effects occurred at the molecular scale, leaving the morphological features of the constituent polymers almost unaltered.

Assignment of spectral features to specific types of chemical bonds

We first assigned the observed features to specific types of chemical bonds based on energy losses of 5–15 eV, as reported in previous studies. The spectral endmembers

resolved from the datasets with MCR are shown separately for the three polymer species in the energy-loss regions, except the bulk plasmon peaks, to elucidate the features shown in Fig. 5, wherein the characteristic peak positions (i)–(vi) are indicated. The resolved spectral endmembers exhibited shoulders at 5–6 and 8–9 eV and significant broad peaks at ~7 and ~22 eV. The significant broad peaks at ~22 eV represented the $\sigma^*+\pi^*$ bulk plasmons [25], whereas the smaller peaks in the 6–7 eV range (marked as (i) and (iv) in Fig. 5) were attributed to the plasmon resonance of π electrons, as in graphite, but more likely to $\pi-\pi^*$ transitions, as indicated by the presence of a similar peak in both solid- and gas-phase aromatic compounds [26–28]. This peak is a characteristic of C = C sp^2 double bonds and those for conjugated and nonconjugated systems may overlap. The peak intensity increases or decreases with increasing radiation damage via double-bond formation or breakage, respectively. Additional features in the 5–6 eV region, which resulted from irradiation damage (molecular modifications of the carbonyl groups after intramolecular dehydrogenation [18, 26, 27] and cross-linking between the benzene rings and main chain [24], marked as (iii) and (vi) in Fig. 5, respectively), were also considered. Miscellaneous features depending on the polymer species, such as shoulders at 8.5 (C–C σ^* for polyethylene, marked as (ii) in Fig. 5) [18, 26] and 12–15 eV (C–C σ^* or C–H σ^* for polyethylene, which were not prominent), were also observed [18].

NLLS fitting of the spectral features with Gaussians

The spectral feature of each endmember was best expressed as a linear combination of a minimum of five Gaussian peaks by using NLLS fitting. The characteristic features, labeled (i)–(vi) in Fig. 5, were classified into the four groups G2–G5, excluding the bulk plasmon (labeled G1), owing to limitations in energy resolution (1–1.5 eV). G2 comprised similar damage peaks ((iii) and (vi)), whereas G3 comprised indistinguishable C = C double bonds ((i) and (iv)), as shown in Fig. 5, with the initial peak (shoulder) positions \pm their half width at half maxima set as 21.0 ± 3 , 4.5 ± 0.5 , 6.0 ± 0.5 , 8.0 ± 0.5 , and 13.0 ± 0.5 eV for G1 (bulk plasmon), G2, G3, G4, and G5, respectively. The peak positions and FWHM were treated as free parameters, and a typical NLLS fitting result is shown in Fig. 6 (for TPU at 200 kV/100 K). Other fitting results are shown in Fig. S4 in the Supplementary Information. The summaries of the peak positions for G1–G4 and the area ratios of G2/G4 and G3/G4 are shown in Fig. 7a–f for various conditions and endmembers. The background intensities around the energy-loss region of 2–10 eV for 1000 kV were significantly higher than those for 200 kV owing to the extended tails of the ZLP peaks resulting from the higher energy resolution (1.5 eV) at 1000 kV. However, changes in the peak positions (Fig. 7a–d) and

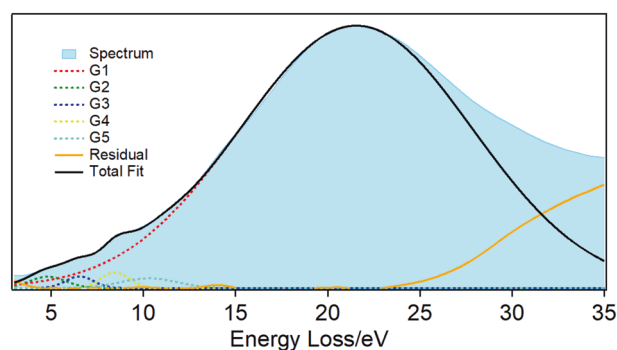


Fig. 6 Results of NLLS fitting with five Gaussians for TPU at 200 kV/100 K

relative peak areas (Fig. 7e, f) for the respective measurement conditions can be discussed without ignoring their physical significance. A summary of the considerations obtained from the analyses done with NLLS fitting is shown in Table 2.

The bulk plasmon peak, G1 (Fig. 7a), provides a measure of the material density for a nearly constant composition because the plasmon energy is proportional to the valence-electron density [7], which is well correlated with the electron MFP for the plasmon loss, which is another measure of the sample thickness. Thus, the plasmon peak position and sample thickness, in units of electron MFP, can be used as fingerprints to distinguish between materials or phases with similar compositions but different densities. In carbon materials such as polymers, σ and π bonds generally provide three and one valence electrons per atom, respectively. Because a monomer has a larger fraction of single σ bonds, it has a higher valence-electron density and exhibits a stronger plasmon peak energy, as seen in Fig. 7a, except at 200 kV/RT. A pseud thickness map in units of electron MFP, λ , for the data obtained at 1000 kV/RT is shown in Fig. 8; this map is very similar to the RGB map obtained under the same conditions, as shown in Fig. 4. Considering that the sample underwent severe thermal damage at 200 kV/RT, the highest plasmon peak positions for all components at this condition were attributed to thermal shrinkage resulting from carbonization/graphitization [29]; this was most evident for LDPE, which exhibited the most prominent $\pi-\pi^*$ transition peak among the four measurement conditions. Notably, the blueshift of the plasmon peak was suppressed more effectively at an accelerating voltage of 1000 kV, even at RT, than at 200 kV/100 K. This finding suggests that the ionization effect caused thermal damage.

The peak position of G2 (Fig. 7b) exhibited no clearly interpretable trends with the measurement conditions investigated, possibly because G2 comprised three or more molecular structures (different types of C = C double bonds), with multiple peaks overlapping at a particular energy resolution, and each component may have behaved differently toward electron irradiation under different conditions. Density functional

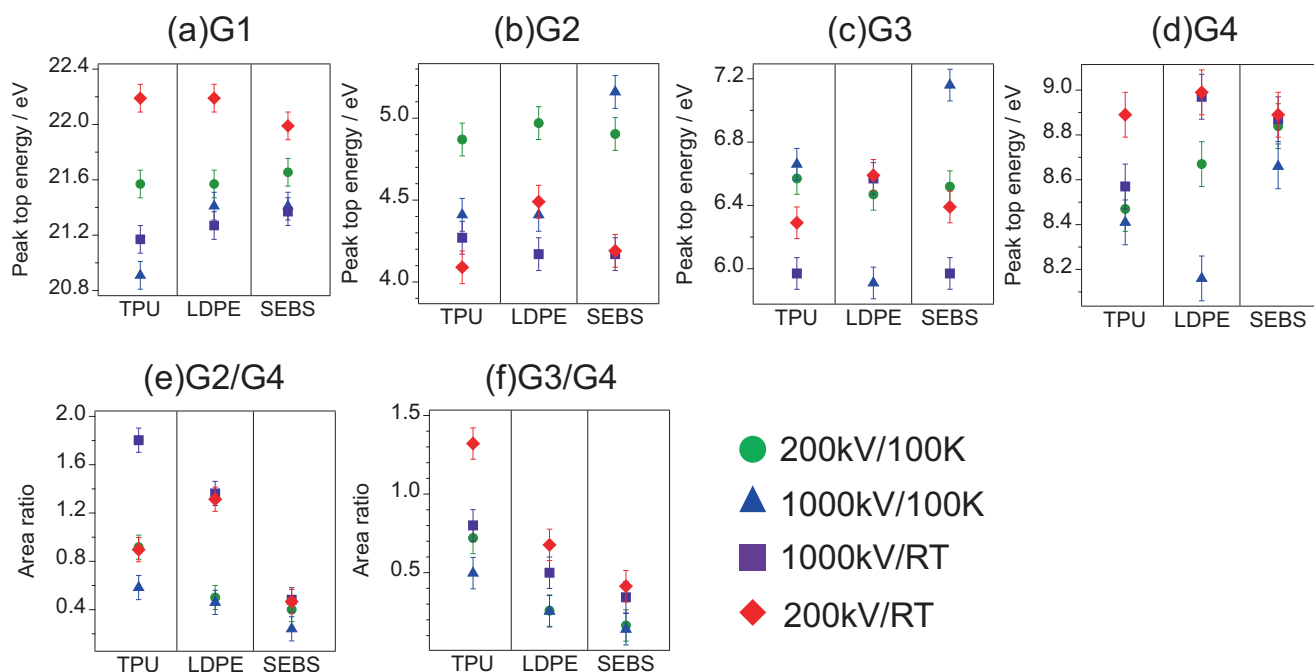


Fig. 7 **a–d** Peak positions obtained via Gaussian fitting under various conditions for peaks G1–G4, respectively. **e, f** Area ratios G2/G3 and G3/G4, respectively

Table 2 Summary of the considerations obtained from analyses of the NLLS fits

Initial structure	Structure or changes caused by irradiation	Conditions prone to occur	Rationale
(i) Benzene-ring	(iii) C = C (Reorganization of the carbonyl group)	1000 kV	G2/G4
(i) Benzene-ring	(vi) Cross-linking	1000 kV	G2/G4
(ii) C-C	(iv) C = C (Nonconjugated)	200 kV	G3, G4 peak shift G3/G4
(ii) C-C	(v) C = C (Conjugated)	200 kV	G3, G4 peak shift G3/G4
–	Graphitization (thermal shrinkage)	200 kV	G1 peak shift

* The Roman numerals correspond to those in Fig. 5

theory (DFT) calculations based on model structures in which the C–C single bonds of the polyethylene chains were transformed into double bonds illustrated that the peak corresponding to the enyl group (corresponding to conjugated double bonds (iv)) shifted toward the higher energy side with an increasing number of double-bond side chains, whereas the peak corresponding to nonconjugated double bonds (corresponding to peak (v)) shifted toward the lower energy side, as shown in Fig. S5 in the Supplementary Information.

The G3 peaks corresponding to TPU and SEBS, as shown in Fig. 7c, were blueshifted for the studies performed at 1000 kV/100 K and 200 kV/100 K compared with those obtained at 1000 kV/RT and 200 kV/RT, presumably because of cross-linking of the benzene rings. In contrast, the G3 peak corresponding to LDPE shifted in the opposite direction from the TPU and SEBS peaks under the of 100 K

and RT conditions, respectively, which can be explained by the conversion of single bonds to double bonds caused by irradiation damage, as theoretically predicted in Fig. S5a in the Supplementary Information.

G4 corresponded to C–C single bonds, and the peak was expected to shift toward the higher energy side owing to conversion of the C–C single bonds to C = C double bonds, as shown in Fig. S5a in the Supplementary Information. As shown in Fig. 7d, the peak positions corresponding to all polymer species were associated with higher energy losses at RT than at 100 K, regardless of the accelerating voltage.

The peak area ratios G2/G4 and G3/G4, as shown in Fig. 7f, g, respectively, indicated alternative aspects of the electron irradiation-induced structural changes. Both ratios had larger values at RT and smaller values at 100 K, except for the G2/G4 ratio for TPU, which showed a significantly

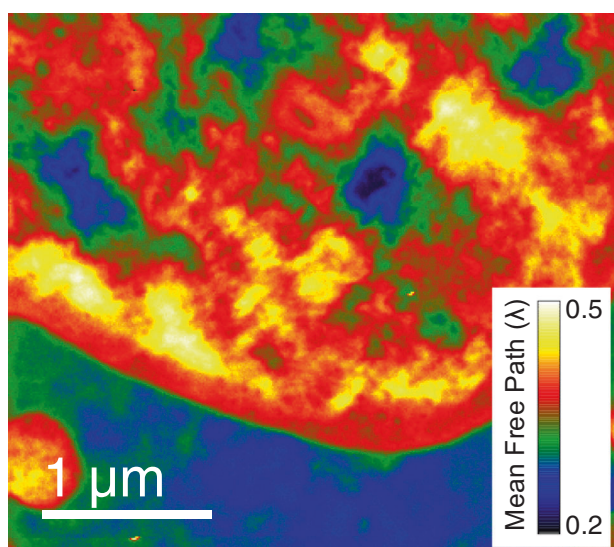


Fig. 8 Pseudo-thickness map of the 1000 kV/RT data in units of electron MFP, λ , for inelastic scattering

higher value at 1000 kV/RT compared with those obtained under the other irradiation conditions. Knock-on damage frequently results in the formation of conjugated double bonds [26] and cross-linked structures [27] between benzene rings and the main chain [30, 31], which may have increased G2/G4. In contrast, due to the thermal damage associated with ionization, G3/G4 was assumed to have increased owing to the formation of nonconjugated C=C double bonds. Thus, G2/G4 and G3/G4 may be indicators for the degrees of knock-on and thermal damage, respectively.

The main factors affecting specimen damage caused by electron irradiation are (a) an increase in temperature due to phonon excitations, (b) ionization due to inelastic electron scattering, (c) direct knock-on between electrons and atomic nuclei, and (d) subsequent secondary diffusion of defects [32]. Factors (a) and (d) can be reduced by cooling the sample [32], and (b) can be suppressed by lowering the inelastic scattering cross-section under high acceleration voltage conditions [33]. Although knock-on damage may be increased at high acceleration voltages [30, 31], (a), (b), and (d) are the dominant factors causing polymer damage [30].

The cross-sections damaged via knock-on and ionization of carbon were estimated with theoretical formulae available in the literature [34, 35]; the results are shown in Figure S6 in the Supplementary Information. Figure S6 indicates that the knock-on damage cross-section at 200 kV was 1.5 times that at 1000 kV, whereas the ionization cross-section at 1000 kV was nearly half of that at 200 kV. Thus, the total electron-irradiation damage may have been reduced significantly by employing an accelerating voltage of 1000 kV.

Based on the differences observed in the characteristic peak positions/area ratios under the 1000 kV/100 K and

200 kV/100 K conditions compared with those obtained under the previously described irradiation conditions, the 1000 kV/100 K and 200 kV/100 K conditions appear to have caused mild irradiation damage. Knock-on damage was more apparent at 1000 kV than at 200 kV, while secondary diffusion of the primary knocked atoms was suppressed at low temperatures, resulting in mitigation of the knock-on damage. In addition, the G3/G4 ratio measured at RT indicated that the extent of thermal damage was lower at 1000 kV than at 200 kV. Thermal damage was mainly associated with the formation of nonconjugated double bonds in the olefinic structure of the main chain [26]. A comparison of the spectral components obtained at 1000 kV/RT or 200 kV/RT and 200 kV/100 K, as shown in Fig. 4b, indicated attenuation of the shoulder at 9 eV, thus suggesting that cooling effectively suppressed ionization, although the thermal damage was more significant for the measurements done at RT.

Conclusions

The results of the proposed STEM-EELS-HSIA method indicated that the original morphologies of the components were retained in the polymer blend, wherein they became nearly miscible at the nanometric scale, with no interfacial reactions. Sample deterioration associated with electron irradiation was insignificant, although severe thermal damage was noted for the 200 kV/RT condition. A maximum spatial resolution of 5 nm may be achieved with the proposed method because of beam overlap between the scan steps, depending on the resistance of the target polymer species to electron-irradiation damage. This resolution is superior to that achievable by scanning transmission X-ray microscopy. Notably, an accelerating voltage of 1000 kV caused less damage than an accelerating voltage of 200 kV, regardless of the temperature, and was more effective for analyzing thicker samples. In the future, the proposed strategy could be refined to generate 3D morphological maps of polymer blends via multiple scans. We will attempt to apply the present method to other types of blends containing a variety of polymer combinations to accumulate a database of their reference low-loss spectra; characteristic features will be assigned to the corresponding chemical formula units, which may contribute to the development of more functional polymers.

Acknowledgements This study was financially supported, in part, by a Grant-in-Aid for Scientific Research (KAKENHI) for Challenging Research (Grant Number 21K18816) from the Japan Society for the Promotion of Science. It was also supported by ‘Advanced Research Infrastructure for Materials and Nanotechnology in Japan (ARIM)’ and ‘Microscopic Imaging Solution Platform in Program for Advanced Research Equipment Platforms’ of the Ministry of Education, Culture, Sports, Science and Technology of Japan.

Compliance with ethical standards

Conflict of interest The authors declare no competing interests.

Publisher's note Springer Nature remains neutral with regard to jurisdictional claims in published maps and institutional affiliations.

Open Access This article is licensed under a Creative Commons Attribution 4.0 International License, which permits use, sharing, adaptation, distribution and reproduction in any medium or format, as long as you give appropriate credit to the original author(s) and the source, provide a link to the Creative Commons license, and indicate if changes were made. The images or other third party material in this article are included in the article's Creative Commons license, unless indicated otherwise in a credit line to the material. If material is not included in the article's Creative Commons license and your intended use is not permitted by statutory regulation or exceeds the permitted use, you will need to obtain permission directly from the copyright holder. To view a copy of this license, visit <http://creativecommons.org/licenses/by/4.0/>.

References

- Parameswaranpillai J, Thomas S, Grohens Y. Polymer blends: state of the art, new challenges, and opportunities. In: Parameswaranpillai J, Thomas S, Grohens Y, editors. *Characterization of polymer blends: miscibility, morphology and interfaces*. Weinheim, Germany: Wiley; 2015. p. 1–7.
- Ougizawa T, Inoue T. Morphology of polymer blends. In: Utracki LA, Wilkie AC, editors. *Polymer blends handbook 2nd edition*. Dordrech, The Netherlands: Springer; 2014. p. 875–918.
- Sawyer CL, Grubb TD, Meyers, FG. Specimen preparation methods. In: *Polymer microscopy*. 3rd ed. New York: Springer; 2008. p. 130–274.
- Trent JS, Scheinbeim JI, Couchman PR. Ruthenium tetroxide staining of polymers for electron microscopy. *Macromolecules* 1983;16:589–98.
- Inamoto S, Shimomura S, Otsuka Y. Electrostatic potential imaging of phase-separated structures in organic materials via differential phase contrast scanning transmission electron microscopy. *Microsc (Oxf)*. 2020;69:304–11.
- Loos J, Sourty E, Lu K, de With G, Bavel Sv. Imaging polymer systems with high-angle annular dark field scanning transmission electron microscopy (HAADF-STEM). *Macromolecules* 2009;42:2581–6.
- Egerton FR. *Electron energy-loss spectroscopy in the electron microscope*. 3rd ed. New York: Springer; 2011.
- Urquhart SG, Hitchcock AP, Smith AP, Ade HW, Lidy W, Rightor EG, et al. NEXAFS spectromicroscopy of polymers: overview and quantitative analysis of polyurethane polymers. *J Electron Spectrosc Relat Phenom*. 1999;100:119–35.
- Matsko NB, Schmid FP, Letofsky-Papst I, Rudenko A, Mittal V. In situ determination and imaging of physical properties of soft organic materials by analytical transmission electron microscopy. *Microsc Microanal*. 2014;20:916–23.
- Dong W, Hakukawa H, Yamahira N, Li Y, Horiuchi S. Mechanism of reactive compatibilization of PLLA/PVDF blends investigated by scanning transmission electron microscopy with energy-dispersive X-ray spectrometry and electron energy loss spectroscopy. *ACS Appl Polym Mater*. 2019;1:815–24.
- Colby R, Williams RE, Carpenter D, Bagués N, Ford BR, McComb DW. Identifying and imaging polymer functionality at high spatial resolution with core-loss EELS. *Ultramicroscopy* 2023;246:113688.
- Hitchcock, PA, Dynes, JJ, Wang, J, Botton, G. Comparison of NEXAFS microscopy and TEM-EELS for studies of soft matter. *Micron*. 2007;09:311–9.
- Almeida PD, Räisänen J. Atomic displacement in solids: analysis of the primary event and the collision cascade. Part I: Neutron and positive ion irradiation. *Eur J Phys*. 2005;26:371–89.
- Pal R, Bourgeois L, Weyland M, Sikder AK, Saito K, Funston AK, et al. Chemical fingerprinting of polymers using electron energy-loss spectroscopy. *ACS Omega*. 2021;6:23934–42.
- Khan MJ, Khan HS, Yousaf A, Khurshid K, Abbas A. Modern trends in hyperspectral image analysis: a review. *IEEE Access*. 2018;6:14118–29.
- Pal R, Sikder AK, Saito K, Funston AM, Bellare JR. Electron energy loss spectroscopy for polymers: a review. *Polym Chem*. 2017;8:6927–37.
- Japanese Patent Application Disclosure. JP2018-193431. p. 2018–193431 A; 2018.
- Varlot K, Martin JM, Quet C, Kihn Y. Towards sub-nanometer scale EELS analysis of polymers in the TEM. *Ultramicroscopy* 1997;68:123–33.
- Cardoso HA, Leite PAC, Galembeck F. Latex particle self-assembly and particle microchemical symmetry: PS/HEMA latex particles are intrinsic dipoles. *Langmuir* 1999;15:4447–53.
- Door R, Gängler D. Multiple least-squares fitting for quantitative electron energy-loss spectroscopy — an experimental investigation using standard specimens. *Ultramicroscopy* 1995;58:197–210.
- de Juan A, Tauler R. Multivariate curve resolution: 50 years addressing the mixture analysis problem – a review. *Anal Chim Acta*. 2021;1145:59–78.
- Braidy N, Gosselin R. Unmixing noisy co-registered spectrum images of multicomponent nanostructures. *Sci Rep*. 2019;9:18797.
- Muto S, Yamamoto Y, Sakakura M, Tian H, Tateyama Y, Iriyama Y. STEM-EELS spectrum imaging of an aerosol-deposited NASICON-type LATP solid electrolyte and LCO cathode interface. *ACS Appl Energy Mater*. 2022;5:98–107.
- Hosoda S, Nozue Y. Molecular structural parameters affecting the lamellar crystal thickness distribution in polyethylene. *Jpn J Polym Sci Technol*. 2014;71:483–9.
- Reznik B, Fotouhi M. Electron microscopy and electron-energy-loss spectroscopy study of crack bridging in carbon-carbon composites. *Compos Sci Technol*. 2008;68:1131–5.
- Ritsko JJ. Electron energy loss spectroscopy of pristine and radiation damaged polyethylene. *J Chem Phys*. 1979;70:5343–9.
- Singh P, Venugopal BR, Nandini DR. Effect of electron beam irradiation on polymers. *J Mod Mater*. 2018;5:24–33.
- Koch EE, Otto A. Characteristic energy losses of 30 keV-electrons in vapours of aromatic hydrocarbons. *Opt Commun*. 1969;1:47–9.
- Oberlin A. Carbonization and graphitization. *Carbon* 1984;22:521–41.
- Liao Y. Damage of materials due to electron irradiation. In: *Practical electron microscopy and database – an online book*. 2006. <https://www.globalsino.com/EM/page4543.html>. Accessed 28 Dec 2022.
- Egerton FR. Mechanisms of radiation damage in beam-sensitive specimens, for TEM accelerating voltages between 10 and 300 kV. *Microsc Res Tech*. 2012;22099:1550–6.
- Suenaga K, Koshino M, Liu Z, Sato Y, Jin C. Single molecular imaging by HR-TEM. *KENBIKYO*. 2010;45:31–5.
- Murata K, Shigemoto R. High voltage electron microscopy in biology. *Microscopy* 2012;46:170–4.
- Clinard FW Jr, Hobbs LW. Radiation effects in Non-Metals. In: Johnson AR, Orlov NA, editors. *Physics of radiation effects in crystals*. 1st ed. The Netherlands: Elsevier B. V.; 1986. p. 387–471.
- McKinley WA Jr, Feshbach H. The Coulomb scattering of relativistic electrons by nuclei. *Phys Rev*. 1948;74:1759–63.